Nonholonomic Modeling of Needle Steering

Robert J. Webster III, Noah J. Cowan, Gregory Chirikjian, and Allison M. Okamura

Department of Mechanical Engineering
The Johns Hopkins University
{robert.webster,ncowan,aokamura,gregc}@jhu.edu
http://www.me.jhu.edu/

Abstract. As a flexible needle with a bevel tip is pushed through soft tissue, the asymmetry of the tip causes the needle to bend. We propose that, by using nonholonomic kinematics, control and path planning, an appropriately designed needle can be steered through tissue to reach a specified 3D target. Such steering capability will enhance targeting accuracy and markedly improve outcomes for percutaneous therapies, facilitate research on therapy effectiveness, and enable new minimally invasive techniques. In this paper, we consider a first step toward active needle steering: design and experimental validation of a nonholonomic model for steering flexible needles with bevel tips. The model generalizes the standard three degree-of-freedom (DOF) nonholonomic bicycle model to 6 DOF using Lie group theory. Model parameters were fit using experimental data, which were acquired via a robotic device designed for the specific purpose of inserting a flexible needle. The resulting parametric fit quantitatively validates the bevel tip needle steering model, enabling future research in flexible needle path planning, control and simulation.

1   Introduction

Needle insertion is perhaps the most widespread surgical technique in existence. It is a critical aspect of many medical diagnoses, treatments and scientific studies, including percutaneous procedures requiring therapy delivery to or sample removal from a specific location. However, errors in needle targeting can mitigate the effectiveness of diagnosis or therapy. Biopsies, for example, cannot completely rule out malignancy due to inaccuracy in positioning the needle tip. Also, radioactive seeds in prostate brachytherapy are often placed at locations substantially different than those pre-planned for optimal dosage. In this work, we focus on modeling the needle bending that occurs due to tip asymmetry. Control and planning based on such a model can compensate for targeting disturbances due to needle bending, error in insertion angle, and tissue deformation.

A kinematic model of needle steering allows one to draw on the many path planning techniques developed by the robotics community. Judiciously chosen paths will allow needles to reach small targets in locations that are inaccessible via straight trajectories. This will expand range of procedures that can be accomplished minimally invasively, requiring fewer open surgeries. Needle steering also has the potential to expand new arenas of clinical research, allowing accurately and precisely targeted injection of new drugs, genetic agents, ablative and cryoablative treatments, etc. Accurate targeting is essential in such clinical research, because it must be verified that

results and outcomes are due to differences in the therapy itself, and not a result of the targeting of the therapy. Needle bending models will also aid in the development of realistic needle insertion simulators for therapy planning and training.

While the needle insertion modeling community has generally regarded the effect of bevel tip asymmetry as an unwanted source of error, it is interesting to note that in clinical practice, some surgeons do make use of the bevel tip [11]. They use it both for steering the needle and aiming injected fluids (the fluid will flow outward at an angle from the bevel). Surgeons accomplish this from experience, making it difficult to teach and limiting accuracy to that of human hand/eye coordination.

Early work in needle modeling and simulation involved recording the forces applied to a needle during insertion and playing back "haptic recordings" or simple force vs. position models in a force-feedback virtual environment [2,7,8]. More recently, researchers have used reality-based needle/tissue interaction modeling to generate models used for planning and simulation [1,4,14]. The effects of needle bending have been explored by several groups. O'Leary, *et al.* [13] demonstrated experimentally that needle bending forces are significantly affected by the presence of a bevel tip. Others have generated needle bending using different strategies such as incorporating a pre-bent stylus inside a straight canula [6], or a telescoping double canula where the internal canula is pre-bent [3]. Kataoka, *et al.* [9] attempted to create a model for needle deflection, but did not account for the bevel tip and admit that the bevel is likely the main source of deflection.

There is only one previous study that has analyzed needle paths from a kinematic viewpoint. DiMaio and Salcudean [5] formulate a needle Jacobian that describes tip motion due to needle base motion and a tissue finite element model. However, their work does not explore the effect of tip asymmetry. Their needle is stiff relative to the tissue, and steering is accomplished by pulling on and angling the needle shaft outside the body to cause the tissue to move. Our approach contrasts theirs in that we consider a system where the needle is flexible relative to the tissue, and does not displace a large amount of tissue in order to steer itself. Ultimately, we expect that a combination of these methods will be most accurate in controlling and describing needle insertions into actual soft tissue.

2 Modeling of Needle Steering

Consider a bevel tip needle driven with two velocity inputs, insertion speed and rotation speed, actuated from the base of the needle. As the needle is inserted into tissue, the tissue imposes a reaction force on the bevel that deflects the needle tip, causing it to follow an arc. Neglecting torsional compliance of the needle, the rotational input at the base causes the needle to turn about its shaft, reorienting the bevel. We model both effects – insertion and rotation – as inputs to a quasi-static nonholonomic system.

For a fixed needle shaft rotation, the model is similar to that of a bicycle with a fixed front wheel angle, ϕ, and fixed distance, ℓ_1, between the front and back wheel, as depicted in Figure 1. A third model parameter, ℓ_2, determines the location along
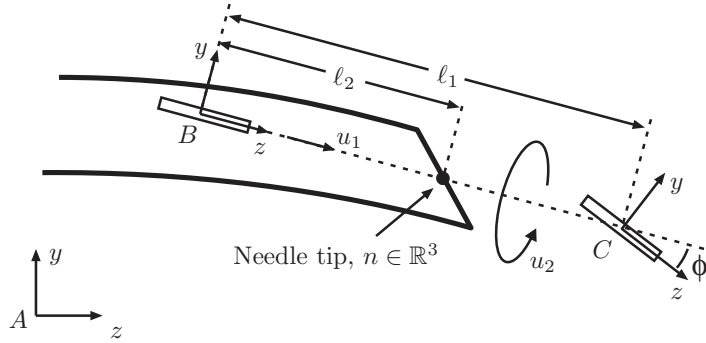
Fig. 1. Configuration of a bevel tipped needle during steering showing the front and back "wheels" at frames B and C of a superimposed bicycle-like nonholonomic model. In this particular configuration, the x-axes for all three frames are pointing into the page.

the bicycle attached to the needle tip, n. The purpose of this study is to determine if the model quantitatively captures the needle steering kinematics. To do so, we fit the model parameters (ϕ, ℓ_1, ℓ_2) experimentally as described in Section 3. We suspect that the model parameters depend on many factors such as tissue stiffness, needle stiffness and bevel angle, but we leave this hypothesis for future investigation.

2.1   Notation and Definitions

Ultimately, we seek to use the two control inputs, insertion and rotation, to drive a needle to a desired position and orientation in six degrees of freedom (DOF). Since generalized coordinates (such as $(x, y, z, \text{roll}, \text{pitch}, \text{yaw})$), have singularities, we resort to a coordinate-free representation of the kinematics. Fortunately the kinematic needle equations are quite simple in the coordinate-free representation, but the convenience and generality comes at the added expense of the formalism and notation presented in this section. We follow the conventions in [12].

Consider the three reference frames depicted in Figure 1: a stationary world frame, A, and two "body" frames, B and C, attached to the needle tip. Using the homogeneous matrix representation, let

$$g_{ab} = \begin{bmatrix} R_{ab} & p_{ab} \\ 0^T & 1 \end{bmatrix} \in \mathrm{SE}(3) \quad \text{where} \quad R_{ab} \in \mathrm{SO}(3),\ p_{ab} \in \mathbb{R}^3$$

denote the rigid transformation between A and B. Likewise, let $g_{bc} = (R_{bc}, p_{bc}) \in \mathrm{SE}(3)$ denote the transformation between B and C.

The isomorphism $\mathbb{R}^3 \simeq \mathfrak{so}(3)$ is defined by

$$\widehat{} : \begin{bmatrix} \omega_1 \\ \omega_2 \\ \omega_3 \end{bmatrix} \mapsto \begin{bmatrix} 0 & -\omega_3 & \omega_2 \\ \omega_3 & 0 & -\omega_1 \\ -\omega_2 & \omega_1 & 0 \end{bmatrix} \in \mathfrak{so}(3), \quad {}^\vee : \begin{bmatrix} 0 & -\omega_3 & \omega_2 \\ \omega_3 & 0 & -\omega_1 \\ -\omega_2 & \omega_1 & 0 \end{bmatrix} \mapsto \begin{bmatrix} \omega_1 \\ \omega_2 \\ \omega_3 \end{bmatrix},$$

where $\mathfrak{so}(3)$ is the Lie algebra of $SO(3)$. It will be convenient to "overload" the definitions of $\widehat{}$ and $\vee$ for $\mathfrak{se}(3)$, the Lie algebra of $SE(3)$. In other words, if $(v, \omega) \in \mathbb{R}^6$, then

$$
\widehat{}: \begin{bmatrix} v \\ \omega \end{bmatrix} \mapsto \begin{bmatrix} \hat{\omega} & v \\ 0^T & 0 \end{bmatrix} \in \mathfrak{se}(3), \quad \vee: \begin{bmatrix} \hat{\omega} & v \\ 0^T & 0 \end{bmatrix} \mapsto \begin{bmatrix} v \\ \omega \end{bmatrix}.
$$

Given two frames, X and Y, related by the rigid transformation $g_{xy} \in SE(3)$, the body-frame velocity between them is given by

$$
V_{xy}^b = \begin{bmatrix} v_{xy}^b \\ \omega_{xy}^b \end{bmatrix} = (g_{xy}^{-1} \dot{g}_{xy})^\vee, \quad \text{where} \quad \begin{aligned} v_{xy}^b &= R_{xy}^T \dot{p}_{xy}, \\ \omega_{xy}^b &= (R_{xy}^T \dot{R}_{xy})^\vee. \end{aligned}
$$

Given three frames A, B and C moving relative to each other, their body velocities are related by $V_{ac}^b = \mathrm{Ad}_{g_{bc}^{-1}} V_{ab}^b + V_{bc}^b$, where

$$
\mathrm{Ad}_g = \begin{bmatrix} R & \hat{p}R \\ 0 & R \end{bmatrix}
$$

is the Adjoint operator for a rigid transformation $g = (R, p) \in SE(3)$.

The unit vectors $e_1, e_2, e_3 \in \mathbb{R}^3$ are the standard basis.

2.2   Nonholonomic Constraints and Control Inputs

Frames B and C are rigidly connected with parallel x-axes, such that the origin of C is a distance ℓ_1 along the z-axis of B. The y-z plane of C is rotated by angle ϕ about the x-axis, as shown. Thus $R_{bc} = e^{\hat{e}_1 \phi}$ and $p_{bc} = \ell_1 e_3$, where ϕ and ℓ_1 are constants to be determined experimentally as described in Section 3.

There are four Pfaffian constraints, because the velocity of the origin of frame B cannot have a projection along the B frame x-axis or y-axis, and the velocity of the origin of frame C cannot have a projection along the C frame x-axis or y-axis. In other words:

$$
e_1^T v_{ab}^b = e_2^T v_{ab}^b = e_1^T v_{ac}^b = e_2^T v_{ac}^b = 0.
$$

Since frames B and C are fixed with respect to each other, $V_{bc}^b = 0$. Thus $V_{ac}^b = \mathrm{Ad}_{g_{bc}^{-1}} V_{ab}^b + V_{bc}^b = \mathrm{Ad}_{g_{bc}^{-1}} V_{ab}^b$, and we have

$$
\underbrace{\begin{bmatrix} 1 & 0 & 0 & 0 & 0 & 0 \\ 0 & 1 & 0 & 0 & 0 & 0 \\ 1 & 0 & 0 & 0 & \ell_1 & 0 \\ 0 & \cos\phi & \sin\phi & -\ell_1\cos\phi & 0 & 0 \end{bmatrix}}_{A} V_{ab}^b = 0.
$$

Assuming $\ell_1 \neq 0$ and $\phi \in (0, \pi/2)$, a basis V_1, V_2 for the right nullspace of A defines the two allowable directions:

$$
V_1 = \begin{bmatrix} v_1 \\ \omega_1 \end{bmatrix} = \begin{bmatrix} e_3 \\ \frac{\tan\phi}{\ell_1} e_1 \end{bmatrix}, \quad V_2 = \begin{bmatrix} v_2 \\ \omega_2 \end{bmatrix} = \begin{bmatrix} 0_{3\times 1} \\ e_3 \end{bmatrix}.
$$

The vector V_1 corresponds to pure needle insertion, while V_2 corresponds to pure needle shaft rotation.

Since we assume the needle shaft is held in place by the surrounding tissue, the effect of the shaft is to replicate needle base control inputs at the tip. Let $u = (u_1, u_2)$ denote the control inputs, where u_1 is the insertion speed, and u_2 is the shaft rotation speed. This leads to the following kinematic model:

$$V_{ab}^b = u_1 V_1 + u_2 V_2, \quad \text{or, equivalently} \quad \dot{g}_{ab}(t) = g_{ab}(t)(u_1 \widehat{V_1} + u_2 \widehat{V_2}). \quad (1)$$

and

$$n(t) = R_{ab}(t)\ell_2 e_3 + p_{ab}(t). \tag{2}$$

Note that the constraint matrix A is independent of g_{ab}, and thus the control vector fields are left-invariant. The system (1) is nonholonomic, since the distribution $\Delta = \text{span}\{V_1, V_2\}$ is not involutive. This can be seen by taking the first Lie bracket

$$V_3 = [V_1, V_2] = (\widehat{V_1}\widehat{V_2} - \widehat{V_2}\widehat{V_1})^\vee = \begin{bmatrix} 0_{3\times1} \\ -\frac{\tan\phi}{\ell_1}e_2 \end{bmatrix},$$

which is linearly independent of V_1 and V_2 (and thus Δ is not involutive). Successive Lie brackets reveal that the system is of nonholomy degree 4, with a relative growth vector of $(2, 1, 2, 1)$ (see [12], Chapter 7). This suggests that this system is controllable, but we leave needle control and steering to future work.

2.3   Discrete Model

A discrete implementation of the kinematic model (1-2) enables simulation and visualization. Advancing the homogeneous transformation, g_{ab}, along V_{ab}^b for T seconds for each time step, $k = 0, 1, 2, \ldots$, yields the discrete-time model

$$\begin{aligned} g_{ab}(k+1) &= g_{ab}(k)e^{(u_1(k)\widehat{V_1} + u_2(k)\widehat{V_2})T} \\ n(k) &= R_{ab}(k)\ell_2 e_3 + p_{ab}(k). \end{aligned} \tag{3}$$

The control inputs $u_1(k)$ and $u_2(k)$ now denote the insertion distance and change in rotation angle, respectively, at step k.

3   Experimental Validation

3.1   Materials

A needle driving mechanism (Figure 2) was designed to control both insertion (u_1) and rotation (u_2) speeds. The insertion subassembly drives the needle by grasping it on the barrel using two opposing rubber wheels actuated by a worm gear attached to a motor. Rotation of the needle about its axis is achieved by rotating the insertion subassembly as a unit. Since the wheels grasp the needle tightly by the barrel,
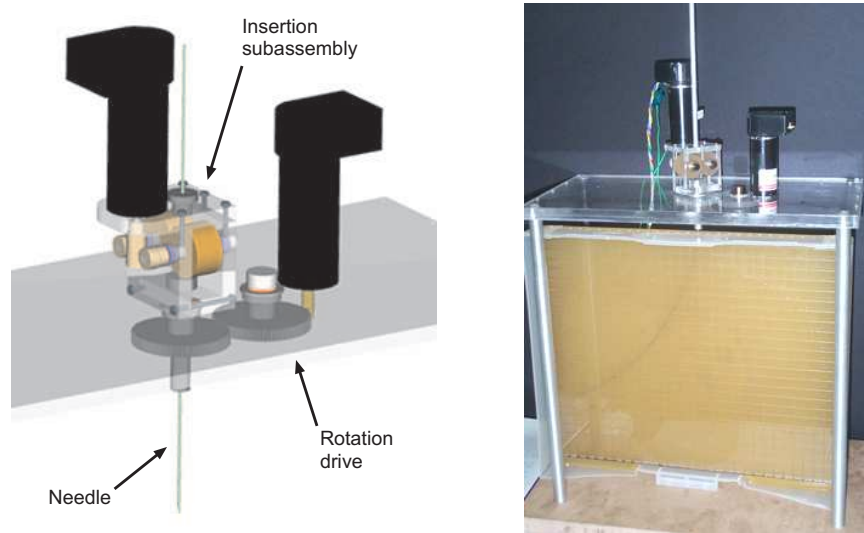
Fig. 2. A needle driving mechanism for steering of flexible needles: CAD model (left) and experimental assembly (right).

rotating the subassembly causes the needle to rotate as well. A slotted needle guide (shown only in the photograph) further fixes the orientation of base of the needle, and thus the bevel direction, relative to the drive wheels. This prevents unwanted needle rotation as the drive wheels turn. Buckling is prevented by passing the needle through a 1.5 mm hole drilled through the aluminum rod that supports the insertion subassembly. This rod extends to the surface of the phantom tissue into which the needle is inserted.

The needle used in the experiments was a 0.7 mm diameter solid Nitinol cylinder (simulating a 22 gauge needle) with a smooth surface finish and a hand-machined bevel tip of 45°. The phantom tissue material used in this experiment was Simulated Muscle Ballistic Test Media from Corbin, Inc. This material was specifically chosen to be stiff (4.9 N/mm by a blunt indentation test) to fit our modeling assumption that the tissue is stiff enough relative to the needle that macroscopic displacement of the tissue by the needle will not occur. That is to say, the needle shaft will follow the trajectory of the tip position. The rubber-like Ballistic Test Material was cast into a sheet approximately 15 mm thick, and the needle was introduced vertically.

To collect coordinates describing the needle path in each insertion, a physical grid was overlaid on the phantom tissue. The 1 cm square grid was laser etched into a clear polycarbonate sheet so that digital photographs could be taken of the needle path through the grid (Figure 2). Coordinates of the needle path were recorded from the digital photographs for each insertion using the physical grid. One data point was recorded for each discrete z value (in 1 cm increments). The y values were recorded

to within ± 1 mm. The nonholonomic model was fit to the data as described in the following section.

3.2   Experimental Procedure

The needle described previously was inserted multiple times into a single phantom tissue sample for all experiments. Care was taken to insert the needle at a different location each time so that the holes cut by previous experiments would not affect the needle path. The rotation of the bevel was maintained by putting a human in the loop (for the rotation degree of freedom only) who watched the needle and minimized out of plane motion by rotating the bevel slightly as necessary. Sources of error in these experiments include initial insertion angle from vertical, human servoed (approximately constant) spin angle, slippage of drive wheels relative to the shaft (not visually perceptible), small deformations of the phantom tissue, and identification of points on the needle path in digital images.

Two sets of input parameters were used in the experimental insertions. In one, u_2 was set to zero, and the needle was inserted at a constant u_1 to a depth of 235 mm. This created a "single bend" insertion profile. In the other, u_2 was set to zero for the first 1/3 of the total insertion depth (83.3 mm). u_1 was then set to zero and the needle was rotated 180 degrees. Finally, with u_2 again fixed at zero, the needle was inserted the remaining 2/3 of the insertion depth at constant u_1, until the needle reached a total insertion depth of 250 mm. This created an S-shaped or "double bend" insertion profile. A total of 13 insertions were performed, composed of eight single bend insertions and five double bend insertions.

When the insertion speed u_1 is constant and needle rotation does not change ($u_2 = 0$), the needle tip follows a circular arc that is a function of the parameters $w = (\phi, \ell_1, \ell_2)$:

$$y = f_w(z) = \sqrt{r_w^2 - (z - a_w)^2} + b_w$$

where the arc center (a, b) and radius r are straightforward functions of the parameters, w. The model can then be fit to the experimental data by minimizing the mean squared error (MSE) cost function:

$$\text{MSE}(w) = \frac{1}{n} \sum_{i=1}^{n} \left(y_i - f_w(z_i) \right)^2. \tag{4}$$

Matlab's `fminsearch` command minimizes a cost function via unconstrained nonlinear optimization according to the Nelder-Mead Simplex Method [10]. To fit all 13 trials simultaneously, the above cost function (4) was modified to include two unique nuisance parameters for each individual trial. These parameters were x_o (the x entry point of the needle) and θ (the initial angle of needle in the y-z plane). The θ parameter was included because it was observed that while all insertions had similar basic shape and curvature properties, they differed by a slight angle in rotation in a manner indicative of a small amount of error in initial entry angle. This error was probably caused by the needle tip deforming the surface of the rubber slightly before puncturing it, and deflecting itself a small amount in the process.
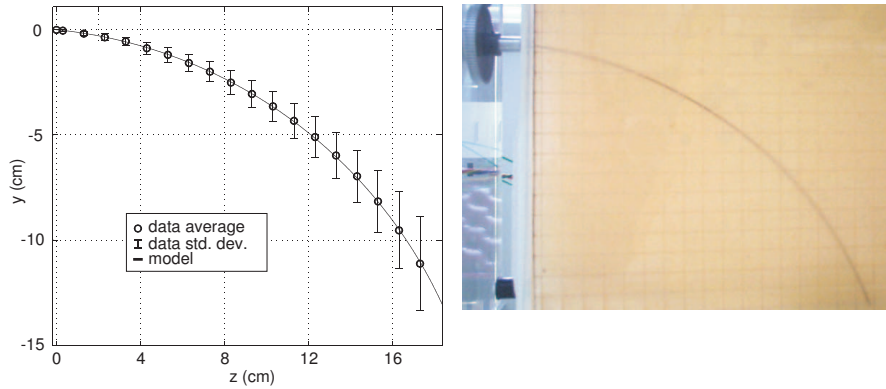
Fig. 3. (Left) The nonholonomic model fit to the average single bend experimental needle path. (Right) During the experiment, the needle was inserted 23.5 cm, without spin.
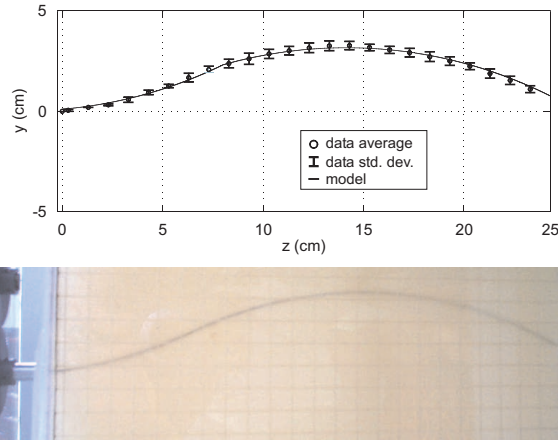

Fig. 4. (Top) The nonholonomic model fit to the average double bend experimental needle path. (Bottom) During the experiment, the needle was inserted 8.3 cm, spun 180°, then inserted another 16.7 cm.

3.3   Results

The experimentally fit parameters were $\phi = 9.96^o$, $\ell_1 = 3.96$ cm and $\ell_2 = 2.03$ cm. Figures 3 and 4 show plots of the single bend and double bend fitted models along with mean data values and standard deviation bars for each data point. Note that the error bars are for raw data and do not include fitted nuisance parameters. This explains why they grow as the needle progresses into the tissue, since the initial angle offset, θ, has a greater effect at greater depth. To create the plots, nuisance parameters for the mean insertion data were generated using the same method originally used to fit the model to the data, but with (ϕ, ℓ_1, ℓ_2) held constant.

As shown in Figures 3 and 4, the model qualitatively fits the data well. This can also be seen quantitatively in that the MSE over all 13 insertions was 9.8 mm^2. This corresponds to a y error of ± 3.1 mm per data point, which is quite low. Nevertheless, the error is somewhat above the measurement error of ± 1 mm, so clearly there is some inherent variability in the data not captured by our kinematic model.

While these results reveal excellent agreement between the model and experimental data, several specific improvements to the experimental and model fitting methods are possible, and are the subject of future investigation. First, we are not able to accurately control the spin of the needle tip (u_2) by adjusting the rotation of the needle base because of the finite torsional stiffness of the needle shaft. We hypothesize that this issue can be overcome by controlling torque. That is, if the needle tip and base are at the same angle, the torque in the shaft will be zero. To enable this, we plan to add a torque sensor to the drive mechanism and implement a controller to obtain the desired shaft rotation. Second, the method for measuring the position of the needle tip as it travels through the tissue can be improved. Currently, we measure points along the needle shaft after the needle has reached its final position. However, this may not precisely reflect the actual path of the needle tip due to shaft stiffness and phantom tissue deformation. Third, it will be useful to more fully understand and assess the quality of the local minima of the cost function, since several parameter combinations appear to fit the data with nearly equal success. This can be an advantage in terms of fast convergence, or a drawback if the optimization is not initialized near a "good" solution.

4   Conclusion and Future Work

A first step in steering a needle to a desired location inside the human body is a kinematic analysis of the needle path. This paper introduces a 6 DOF nonholonomic model based on steering due to bevel tip asymmetry. Using a robotic mechanism designed for flexible needle insertion, we demonstrated that our model accurately predicts the path of a compliant needle through relatively stiff phantom tissue.

This work facilitates a broader study to improve the accuracy of needle targeting for clinical and research applications. Future research activities include: (1) determining the relationship of the bevel angle to the steering angle ϕ, (2) creating a noise model that captures the inherent variability of needle insertion, (3) integrating this needle steering model into simulations that include tissue deformation [1,4,5], (4) path planning for steering needles around obstacles (e.g., bones, delicate structures, etc.) in order to acquire targets not previously accessible, (5) selection of optimal insertion points, and (6) development of a robotic system for needle steering that uses feedback from medical imaging to enhance accuracy in the presence of unmodeled tissue deformation and inhomogeneity.

References

1. R. Alterovitz, J. Pouliot, R. Taschereau, I-C Hsu, and K. Goldberg. Sensorless planning for medical needle insertion procedures. *IEEE/RSJ International Conference on Intelligent Robots and Systems*, pages 3337–3343, 2003.
2. P. N. Brett, A. J. Harrison, T. A. Thomas, and A. Carr. Simulation of resistance forces acting on surgical needles. *Proceedings of the Institution of Mechanical Engineers*, 211 (H4):335–347, 1997.
3. W. Daum. A deflectable needle assembly, 2003. Patent 5,572,593.
4. S. P. DiMaio and S. E. Salcudean. Needle insertion modeling and simulation. *IEEE Transactions on Robotics and Automation*, 19(5):864–875, 2003.
5. S. P. DiMaio and S. E. Salcudean. Needle steering and model-based trajectory planning. *Medical Image Computing and Computer-Assisted Intervention*, pages 33–40, 2003.
6. R. Ebrahimi, S. Okzawa, R. Rohling, and S. E. Salcudean. Hand-held steerable needle device. *Medical Image Computing and Computer-Assisted Intervention*, pages 223–230, 2003.
7. P. Gorman, T. Krummel, R. Webster, M. Smith, and D. Hutchens. A prototype haptic lumbar puncture simulator. *Proceedings of Medicine Meets Virtual Reality*, pages 106–109, 2000.
8. L. Hiemenz, J. S. McDonald, D. Stredney, and D. Sessanna. A physiologically valid simulator for training residents to perform an epidural block. *Proceedings of the IEEE Biomedical Engineering Conference*, pages 170–173, 1996.
9. H. Kataoka, T. Washio, M. Audette, and K. Mizuhara. A model for relations between needle deflection, force, and thickness on penetration. *Medical Image Computing and Computer-Assisted Intervention*, pages 966–974, 2001.
10. J. C. Lagarias, M. H. Wright, and P. E. Wright. Convergence properties of the nelder-mead simplex method in low dimensions. *SIAM Journal of Optimization*, 9(1):112–147, 1998.
11. K. Murphy. Department of Radiology, The Johns Hopkins Medical Institutions. Personal Communication, 2003.
12. R. M. Murray, Z. Li, and S. S. Sastry. *A Mathematical Introduction to Robotic Manipulation*. CRC Press, Ann Arbor MI, 1994.
13. M. D. O'Leary, C. Simone, T. Washio, K. Yoshinaka, and A. M. Okamura. Robotic needle insertion: Effects of friction and needle geometry. *IEEE International Conference on Robotics and Automation*, 2003. In press.
14. C. Simone and A. M. Okamura. Haptic modeling of needle insertion for robot-assisted percutaneous therapy. *IEEE International Conference on Robotics and Automation*, pages 2085–2091, 2002.